small methods
www.small-methods.com

Revealing the Mechanism Underlying 3D-AFM Imaging of Suspended Structures by Experiments and Simulations

Mohammad Shahidul Alam, Marcos Penedo, Takashi Sumikama,* Keisuke Miyazawa, Kaori Hirahara, and Takeshi Fukuma**

The invention of 3D atomic force microscopy (3D-AFM) has enabled visualizing subnanoscale 3D hydration structures. Meanwhile, its applications to imaging flexible molecular chains have started to be experimentally explored. However, the validity and principle of such imaging have yet to be clarified by comparing experiments and simulations or cross-observations with an alternative technique. Such studies are impeded by the lack of an appropriate model. Here, this difficulty is overcome by fabricating 3D carbon nanotube (CNT) structures flexible enough for 3D-AFM, large enough for scanning electron microscopy (SEM), and simple enough for simulations. SEM and 3D-AFM observations of the same model provide unambiguous evidence to support the possibility of imaging overlapped nanostructures, such as suspended CNT and underlying platinum (Pt) nanodots. Langevin dynamics simulations of such 3D-AFM imaging clarify the imaging mechanism, where the flexible CNT is laterally displaced to allow the AFM probe access to the underlying structures. These results consistently show that 3D-AFM images are affected by the friction between the CNT and AFM nanoprobe, yet it can be significantly suppressed by oscillating the cantilever. This study reinforces the theoretical basis of 3D-AFM for imaging various 3D self-organizing systems in diverse fields, from life sciences to interface sciences.

1. Introduction

Atomic force microscopy (AFM) was originally developed for visualizing 2D surface structures by strongly fixing the sample to the substrate. A sharp tip affixed to a cantilever scans the sample in the XY directions, thereby producing a high-resolution 2D topographical image of the specimen. Despite its remarkable capability to generate surface images with sub-nanometer resolution,[1] the methodology falls short in furnishing crucial 3D information regarding the sample. Moreover, there was a belief that AFM could obtain high-resolution images only when the sample was anchored firmly to a substrate. Although there is a technique that can successfully reconstruct the 3D surface topography of intricate structures from 2D images,[2] this method lacks vertical extension, making it excel at visualizing detailed 3D surface profiles but unsuitable for imaging the internal structures of 3D

M. S. Alam, T. Fukuma
Division of Nano Life Science
Kanazawa University
Kakuma-machi, Kanazawa 920-1192, Japan
E-mail: fukuma@staff.kanazawa-u.ac.jp
M. Penedo
École Polytechnique Fédérale de Lausanne
Institute for Bioengineering
Laboratory for Bio and Nanoinstrumentation
Lausanne CH 1015, Switzerland
E-mail: marcos.penedo@epfl.ch
T. Sumikama, K. Miyazawa, T. Fukuma
WPI Nano Life Science Institute (WPI-Nano LSI)
Kanazawa University
Kakuma-machi, Kanazawa 920-1192, Japan
E-mail: sumi@staff.kanazawa-u.ac.jp
K. Miyazawa, T. Fukuma
Faculty of Frontier Engineering
Kanazawa University
Kakuma-machi, Kanazawa 920-1192, Japan
K. Hirahara
Department of Mechanical Engineering
Osaka University
2-1 Yamadaoka, Suita, Osaka 565-0871, Japan

The ORCID identification number(s) for the author(s) of this article can be found under https://doi.org/10.1002/smtd.202400287

DOI: 10.1002/smtd.202400287

objects. These drawbacks are overcome with the development of 3D-AFM.[3,4]

In 3D-AFM, the tip scans through a multidimensional space, recording forces in both vertical and lateral directions to produce a 3D force map of the sample. It captures time-average density distributions of the surrounding water and surface structures, offering valuable insights into their spatial arrangement. This powerful technique has been employed widely to obtain atomically resolved images of solid-liquid interfaces on various surfaces,[3,5–12] revealing the distinguished molecular structure of liquid in contrast to its arrangement in the bulk region, known as hydration structure. Such imaging is enabled by the self-organization capability of the hydration structure, wherein a tip disturbs the organization during scanning, yet upon removal, the original structure seamlessly recovers due to its self-organization ability. It also visualizes the interfacial hydration structure formed on soft biomolecules such as lipid membranes,[13,14] proteins,[14] or DNA.[15,16] The ability of 3D-AFM to visualize and analyze such fine details has contributed significantly to our understanding of interfacial phenomena and the behavior of liquids at the molecular level. Moreover, the imaging mechanism of hydration structure measurement is well established through the development of the theoretical model and detailed comparison of experimental results with molecular dynamics simulations.[5,8,17–23]

3D-AFM measurements of hydration structures paved the way for exploring structures bestowed with self-organizing capabilities. Thus, researchers from different fields employed this remarkable technique to observe flexible surface structures. Asakawa et al. first visualized the thermally fluctuating lipid headgroups at the lipid-water interface with subnanometer resolution.[13] Later, Suzuki et al. observed hemicylindrical adsorption structures of surfactants on a graphite surface with nanoscale resolution.[24] Recently, Penedo et al. reported the 3D intracellular imaging of living cells by the nanoendoscopy-AFM technique.[25] This approach introduces a sharp AFM nanoprobe inside the living cells and visualizes suspended actin fibers.[25] Furthermore, the 3D configuration of flexible surface structures, including polymers[11,26] and surfactants[27,28] has also been reported. Despite the availability of results related to measuring flexible structures by 3D-AFM, the imaging mechanism is not well established. Fundamentally, the imaging mechanisms of hydration structures and flexible structures are different. In hydration structure measurements, the water moves much faster than the tip. So, we can assume the system is always equilibrated. Thus, its mechanism has been extensively studied based on statistical mechanics theory.[20,21] This theory is not necessarily applicable to the measurements of flexible surface structures, where the tip velocity can be comparable to or faster than the movement of target objects.[29] Therefore, there is a strong demand for clarifying the imaging mechanism of flexible structures by 3D-AFM.

All the previous reports[11,13,24–28] suggest that there is a good possibility of observing the flexible structures by 3D-AFM, but it is not fully convincing due to a poor understanding of the imaging mechanism. The challenge lies also in our inability to confirm or cross-validate the obtained results by other techniques, as other methods lack the capability to produce an image of molecular-scale 3D structures in liquid as 3D-AFM. Moreover, the limited understanding of the target structure forces us to rely on speculation based on the appearance of the structure in the 3D-AFM results. Therefore, it would be ideal to prepare a slightly larger and well-defined 3D model structure that can be observed using other techniques. This would enable a thorough comparison of the results with AFM images and help to interpret the results more precisely, as there would be an accurate understanding of the target sample. In addition, a deep understanding of the model structure enables us to conduct accurate simulations to understand the imaging mechanism of flexible structures.

The flexible structures, being suspended rather than firmly attached to a solid substrate, require being careful during imaging to minimize disturbance. This involves reducing the force, friction, or adhesion exerted by the scanning tip. However, there are currently no studies addressing this aspect, highlighting the need to optimize the ideal conditions for accurate measurements.

In this study, we demonstrate that 3D-AFM can visualize the 3D configuration of vertically overlapped nanoscale structures by imaging a suspended carbon nanotube (CNT) fiber with underlying nanodots, and investigate the mechanism and optimal conditions for such imaging through a combined experimental and computational approach. The fabrication of the 3D CNT model structure was performed by focused ion beam-scanning electron microscopy (FIB-SEM) combined with a nanomanipulation tool. To optimize the conditions for imaging flexible structures, we conducted 3D-AFM measurements of the fabricated model structure in different AFM operational modes (static and dynamic[30]). In addition, we performed the Langevin dynamics simulation of a CNT fiber with an AFM nanoprobe to understand the 3D-AFM imaging mechanism of flexible structure. Furthermore, to provide direct unambiguous evidence supporting the capability of 3D-AFM to visualize vertically overlapped 3D nanostructures, we measured the model CNT structure with the underlying platinum (Pt) nanodots, providing a method to tridimensionally reconstruct the structure of interest from the collected 3D data.

2. Results and Discussion

2.1. Fabrication Method of 3D CNT Model Structure

In this study, we first established a method to microfabricate 3D CNT model structures by FIB-SEM-based tools. For a precise manipulation of the CNTs during the construction of the 3D structure, we used a nanomanipulator integrated within our SEM. **Figure 1a–f** schematically exhibits the fabrication process, and Figure 1g–l shows their corresponding SEM images.

First, multi-walled CNTs with a diameter of a few tens of nanometers were attached to the edge of a silicon (Si) cartridge as shown in Figure 1a. Details about the fabrication process of Si cartridges with CNTs are discussed in the experimental section. A tungsten (W) probe was inserted into the probe holder of the nanomanipulator, positioned at a 45° angle from the surface of the Si cartridge (Figure 1a). The W probe was carefully positioned at the same height as the CNT to facilitate afterward the contact between them, as depicted in the SEM image of Figure 1g. The CNT snapped into the W probe when they came into very close proximity, because of the van der Waals force. To further enhance the joint strength, the Electron Beam Deposition (EBD) technique was employed to deposit carbon through a nearby gas injecting system (GIS) as shown in Figure 1b. The SEM

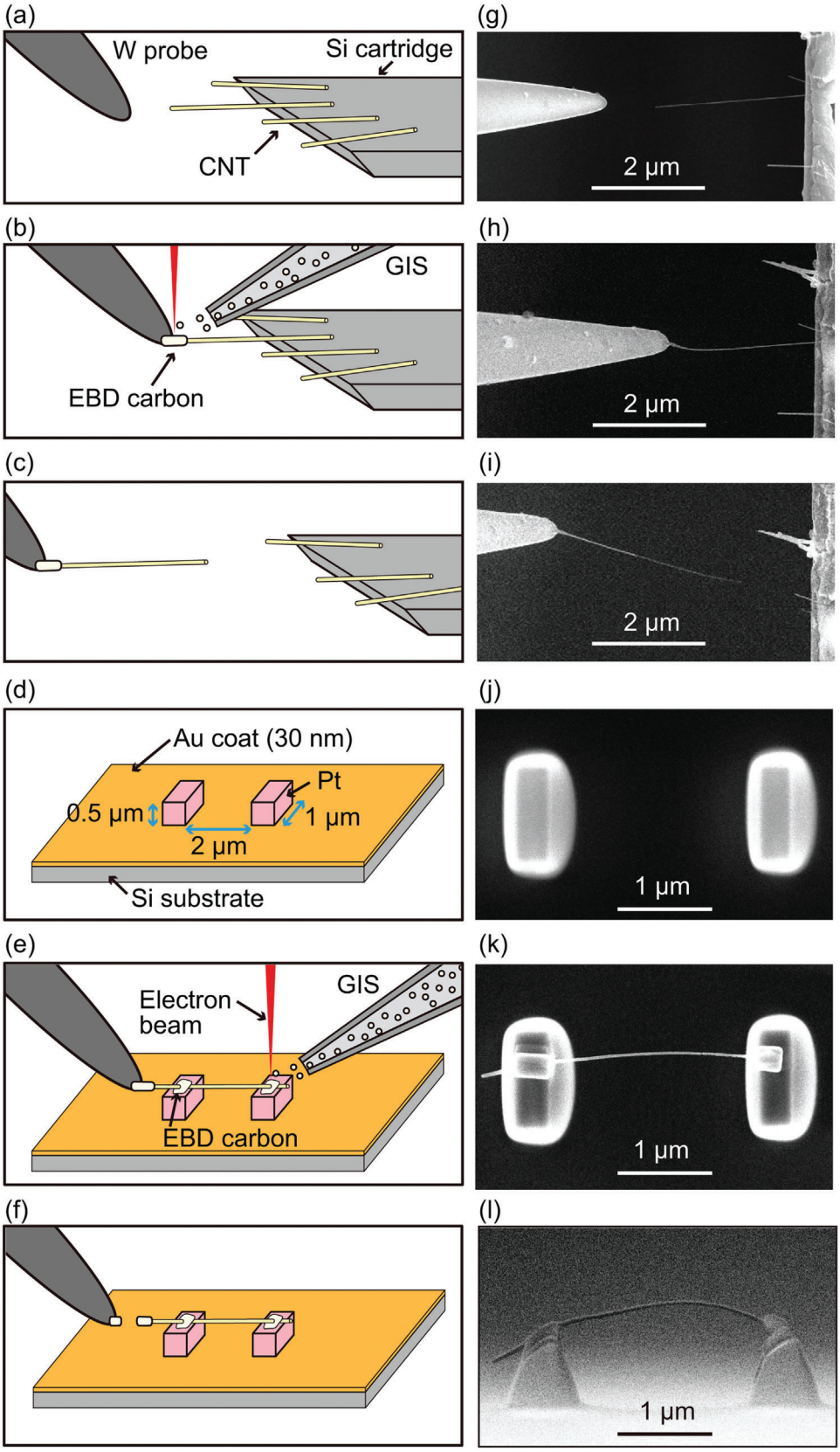

Figure 1. Fabrication method of the 3D CNT model structure. a–f) Schematic illustration of the fabrication process and g–l) their corresponding SEM images.

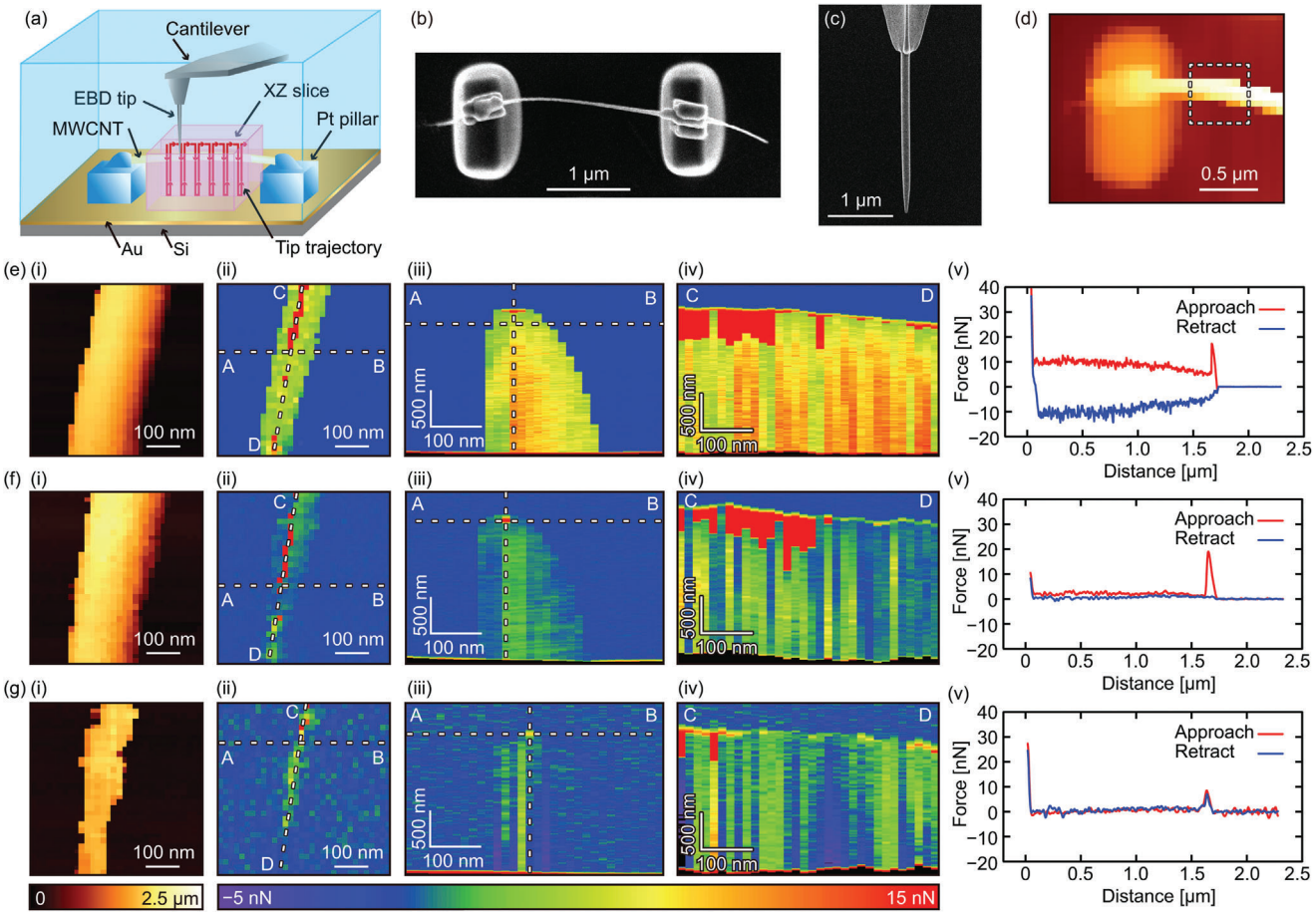

Figure 2. 3D-AFM measurements of the suspended CNT fiber. a) Schematic of the 3D-AFM measurement, where AFM nanoprobe measured the CNT fiber by measuring *F-z* curves within a designated area. SEM image of b) the 3D CNT model structure and c) the carbon EBD nanoprobe used for the 3D-AFM measurement. d) 2D height image simultaneously obtained with 3D force mapping of the CNT model structure. 2D and 1D data derived from the 3D data obtained by the 3D-AFM measurements of the suspended CNT fiber in the different AFM operational modes: e) the static mode, f) the first resonance in dynamic mode, g) the second resonance in dynamic mode. All these experiments were performed in the same region indicated by the white square in (d). i) Contact point maps (see Figure S1, Supporting Information for more details). ii) *xy* cross sections were taken at the vertical position denoted by the horizontal dotted lines in (iii). iii) AB cross sections were obtained perpendicular to the CNT, indicated by line AB in (ii). iv) CD cross sections were obtained along the CNT, indicated by the line CD in (ii). v) *F-z* curves were measured at the position indicated by the vertical dotted line in (iii).

image in Figure 1h illustrates the CNT strongly joined with the W probe following carbon deposition. Afterward, the CNT was gently lifted by the W probe, eventually being detached from the Si cartridge (schematic representation in Figure 1c). The SEM image of Figure 1i depicts the successful pulling of CNT, lying attached to the W probe. In this case, the diameter of the CNT was ≈30 nm. During this process, it is important to pay attention to the pulling direction to avoid any midsection fractures in the CNT.

Subsequently, two rectangular platinum (Pt) pillars were fabricated by the EBD technique on the 30 nm gold-coated Si substrate as illustrated in Figure 1d,j. These pillars were positioned 2 μm apart from each other. The length and thickness of each pillar were 1 and 0.5 μm, respectively. After fabricating Pt pillars, the next step involved carefully positioning the CNT on top of these pillars. With the help of a nanomanipulator, we precisely handle the W probe to establish contact between the CNT and Pt pillars. Right after, we deposited carbon on both contact points to enforce the junction bonding as shown in Figure 1e. Once the CNT was strongly attached, the W probe was carefully withdrawn, allowing the CNT to remain on the pillars, as illustrated in Figure 1f. The SEM image in Figure 1k showcases the 3D CNT model structure on a gold-coated Si substrate, after withdrawing the W probe. The joint between the CNT and Pt pillars should be strong enough to prevent any movement of CNT during the detachment of the W probe. The side view of the structure in Figure 1l confirms that the CNT was suspended above the ground.

2.2. 3D-AFM Measurement of Suspended CNT Fiber

Figure 2a depicts the schematic illustration of the 3D-AFM measurement technique. The 3D CNT model structure shown in Figure 2b was immersed in water for the measurement. We performed the experiment in liquid because 3D self-organizing systems are abundant in the liquid environment. A long carbon

nanoprobe fabricated by the EBD technique on a commercially available silicon cantilever (OPUS 240AC, spring constant: k = 3 N m^{-1}), was used to perform the 3D-AFM measurement of the CNT model by acquiring force versus distance (*F-z*) curves at different positions in the desired area (as schematically shown in Figure 2a). An example of such a nanoprobe is displayed in Figure 2c, where the length is 2.5 µm, a base diameter below 130 nm and a tip radius ≈15 nm. Details about the nanoprobe fabrication process are described in the experimental section. The length of the nanoprobe was sufficient to traverse the CNT and reach the substrate.

Two distinct methods were applied for the 3D-AFM measurements with the aim of optimizing ideal conditions for 3D imaging of suspended structures. These are known as static and dynamic modes. In the static mode, the nanoprobe descends vertically until it reaches the predefined force set point before retracting. Figure 2e presents the 3D-AFM results of suspended CNT fiber obtained in static mode. On the other hand, in the dynamic mode, the nanoprobe descends vertically while simultaneously oscillating the cantilever with a certain amplitude at its resonance frequency. The tip retracts when the cantilever's oscillation amplitude decreases to a certain setpoint. Figure 2f,g depicts the 3D-AFM results of suspended CNT fiber acquired in the dynamic mode by oscillating the cantilever at its first (Figure 2f) and second (Figure 2g) resonance frequencies, respectively.

Figure 2d presents a 2D height image simultaneously obtained with 3D force mapping of the CNT model structure. We selected a small region, highlighted by a white square in Figure 2d, for the measurement of the CNT in different modes for comparison. The illustrations in Figure 2e–g-i depict the surface topography of the CNT obtained through contact point (CP) mapping in various modes of 3D-AFM. (see Figure S1 (Supporting Information) for details about the method of CP mapping). Although there is no significant difference in the CP mapping between static and the first resonance in dynamic modes, a notable reduction in the apparent width is observed at the second resonance in dynamic mode (Figure 2e–g-i). The *xy* cross sections shown in Figure 2e–g-ii are taken at the vertical tip position denoted by the horizontal dotted lines in Figure 2e–g-iii.

The differences in various modes of 3D-AFM operation for measuring the suspended CNT fiber are clear in the AB and CD cross sections (Figure 2e–g-iii,iv). These cross sections were obtained in two orientations: perpendicular to the CNT (AB) and along its length (CD) (Figure 2e–g-ii). During the 3D-AFM imaging, when the tip attempted to reach the substrate by surpassing the CNT, the remarkable flexibility of CNT led to a gentle lateral displacement after a repulsive interaction with the tip to a certain point, allowing the tip to reach the substrate. Once the tip retracts, CNT promptly returns to its initial position. The intense red contrast indicates the position of CNT as the tip required higher forces to overcome the CNT. The contrast observed beneath the CNT arises from lateral friction occurring between the CNT and nanoprobe walls as it progresses toward the substrate. It is clearly visible that lateral friction in the static mode is much higher than in both dynamic modes (Figure 2e–g-iii,iv). Moreover, the second resonance in dynamic mode shows a further reduction in friction compared to the first resonance in dynamic mode (Figure 2g-iii,iv).

This characteristic is also evident in *F-z* curves (Figure 2e–g-v) derived from the AB cross sections at a specific position indicated by the vertical dotted line in Figure 2e–g-iii. After the tip contacts the CNT and continues traveling down toward the surface, the vertical force exerted by the cantilever experiences a gradual rise until the CNT is laterally displaced. This results in a noticeable force drop, a clear signature that the nanoprobe overcame the CNT obstacle. This critical event can be observed in the form of a force peak in the approach curve depicted in Figure 2e–g-v. Then, the cantilever's vertical force exhibits an extended plateau and concludes with a sharp monotonous increase, indicating the tip reached the gold substrate. Subsequently, the tip retracts by a few micrometers, far from the CNT. In the static mode, the presence of a large force offset and minor peaks within the plateau region indicate higher friction between the CNT and nanoprobe walls, which are significantly reduced in both dynamic modes.

Notably, 20 $nm_{p\text{-}p}$ oscillation amplitude was used for exciting the cantilever at the first resonance in dynamic mode which led to lower friction between the CNT and nanoprobe walls compared to the static mode. To understand the potential correlation between oscillation amplitude and friction, we performed the 3D-AFM measurements of the CNT structure by varying the oscillation amplitude at the first resonance in dynamic mode as shown in Figure S2 (Supporting Information), and found that the amplitude over ≈9 $nm_{p\text{-}p}$ is sufficient for reducing the friction.

These results highlight the impact of oscillating the cantilever in dynamic mode, revealing a significant reduction in the nanoprobe's adhesion to the suspended CNT structure. The continuous vibration plays a pivotal role in hindering stable and strong adhesion between the tip and CNT, hence producing lower friction in dynamic mode, facilitating the 3D reconstruction of flexible structures while minimizing potential damage.

2.3. Langevin Dynamics Simulations

To understand the imaging mechanism of a flexible structure with 3D-AFM, we performed the Langevin dynamics simulations for a single CNT fiber and a nanoprobe employing a polymer model, as shown in **Figure 3**. Moreover, in 3D-AFM measurements of the CNT model structure (Figure 2), we interpret that CNT undergoes lateral displacement to facilitate the AFM nanoprobe to reach the substrate. Additionally, we found that the friction between CNT and nanoprobe walls significantly decreased when oscillating the cantilever in dynamic mode. The Langevin dynamics simulation can validate and help to gain deeper insights into these dynamic scenarios. The simulation shown in Figure 3, oscillated the nanoprobe at the same amplitude and frequency as the first resonance in dynamic mode of the experiment, replicating the conditions illustrated in Figure 2f.

The schematic of the simulation model, including the specifications of the nanoprobe, is presented in Figure 3a. The shape of the nanoprobe attempts to replicate the tip used in the experiments. The 2D *xz* cross section generated from the simulation is shown in Figure 3b, where red contrast highlights the position of the CNT. This simulated cross section closely resembles the corresponding experimental cross section AFM image illustrated in Figure 2f-iii.

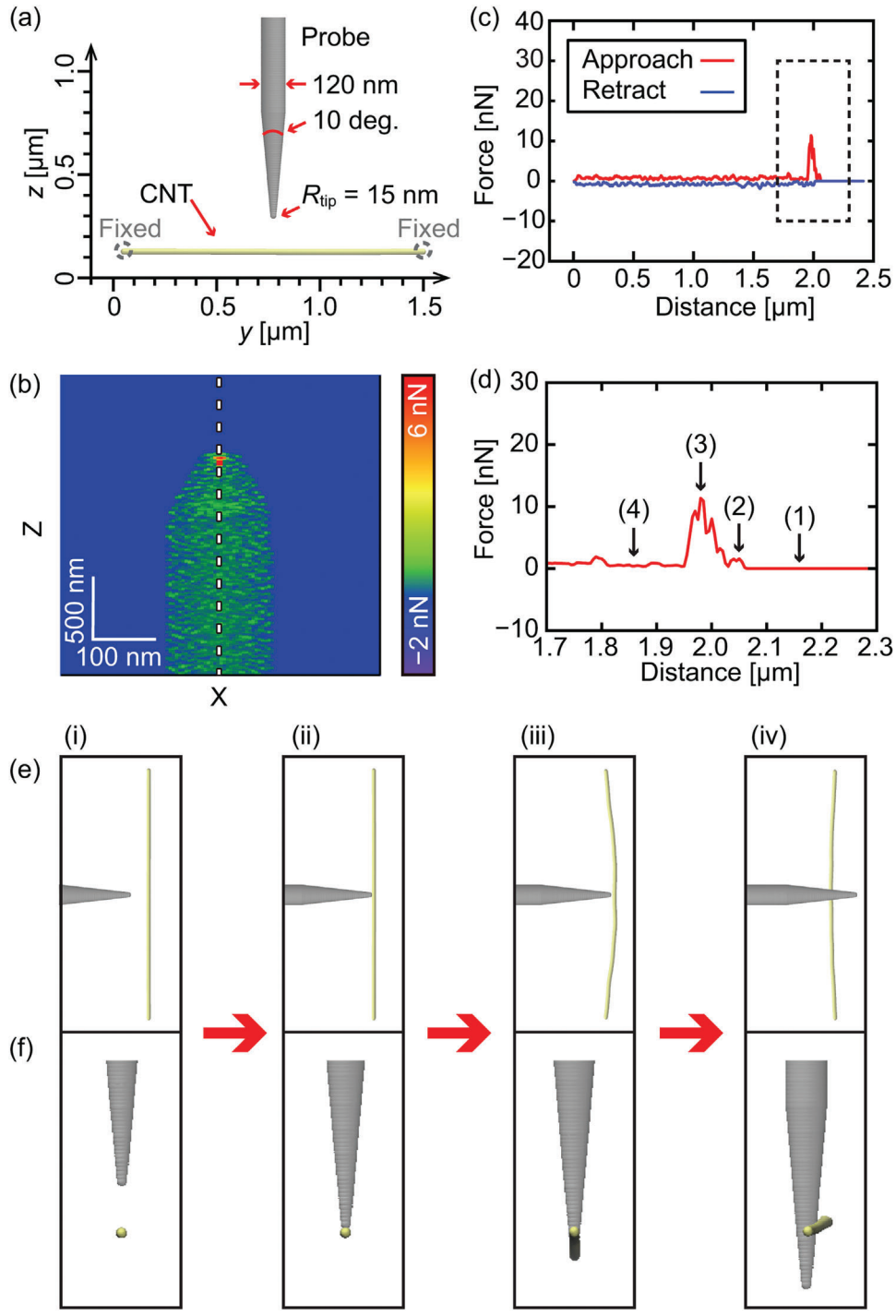

Figure 3. Langevin dynamics simulation of the suspended CNT fiber. a) Simulation model with detailed Information about the nanoprobe. b) *xz* cross section of the 3D-AFM image at the center of CNT, in the dynamic mode. c) *F-z* curve obtained at the position indicated by the vertical dotted line in (b). d) Enlarged view of the *F-z* curve at the region highlighted by the black square in (c), segmented into four sections to understand the interaction between CNT and nanoprobe during imaging. e,f) Front and side views of the snapshots of the simulation model at each of the four sections. i) Nanoprobe approach toward the CNT. ii) Nanoprobe contact with CNT. iii) CNT undergoes bending due to nanoprobe indentation. iv) CNT was laterally displaced and allowed the nanoprobe to reach the substrate.

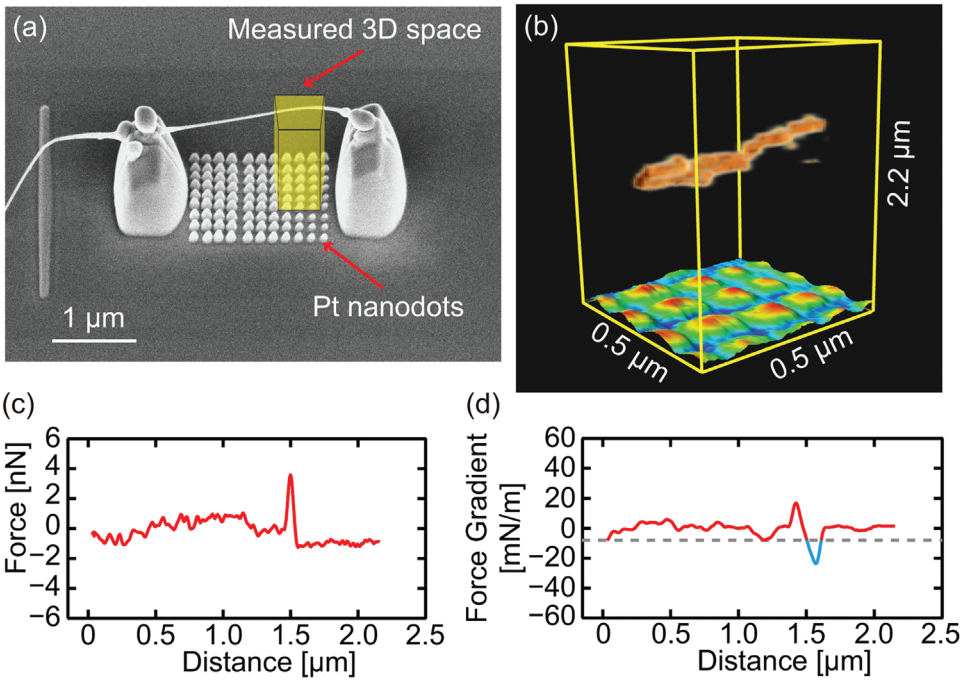

Figure 4. 3D-AFM measurement of the overlapped nanostructures. a) SEM image of the 3D structure with the suspended CNT and Pt nanodots beneath it. b) 3D-AFM map of overlapping nanoscale structures ($0.5 \times 0.5 \times 2.2\ \mu m^3$) obtained at the area highlighted by the yellow box in (a). c) *F-z* curve derived from the measured 3D force map. d) Force gradient versus distance curve obtained by differentiating the curve shown in (c). The region below $-8\ mN\ m^{-1}$ (highlighted by blue color) was extracted and shown in (b) to visualize the CNT.

To elucidate the interaction characteristics as the nanoprobe attempts to pass through the CNT, a single *F-z* curve (Figure 3c) is obtained at the position of the CNT, indicated by the vertical dotted line in the simulated *xz* cross section (Figure 3b). A significant force peak is observed in the approach curve, aligning well with the peak seen in the experimental curve (Figure 2-v) which arises from the interaction between the nanoprobe and CNT. A magnified region around the force peak in the approach curve is presented in Figure 3d, where we categorize this region into four sections indicated by arrows (1)–(4) to provide a more detailed explanation of the interaction between the nanoprobe and CNT. The corresponding snapshots during the four sections from front and side views are presented in Figure 3e,f, respectively.

In the initial phase (i), the nanoprobe is far from the CNT. Thus, there is no observable cantilever deflection or vertical force (arrow (1) in Figure 3d). As the nanoprobe vertically moves down, it establishes contact with the CNT (arrow 2), as shown in Figure 3e,f-ii. From here, the cantilever's vertical force rapidly increases as the nanoprobe continues to descend, as indicated by arrow (3) in Figure 3d. This sudden increase in force results in the bending of the suspended and adequately flexible CNT, as seen in the snapshot in Figure 3e,f-iii. After certain repulsive interactions, the CNT undergoes lateral displacement, as evident in Figure 3e,f-iv. This displacement, in turn, leads to a sharp decrease in the vertical force exerted by the cantilever (arrow 4 in Figure 3d) and allows the nanoprobe to reach the beneath. This validates the explanation provided in Figure 2. As the nanoprobe passes through the CNT fiber, the force reduces significantly (arrow (4) in Figure 3d) which is consistent with the experimental observation (Figure 2f-iv). Moreover, the continuous vibration of the nanoprobe, as seen in Movie S1 (Supporting Information), likely hinders the establishment of the strong adhesion to the CNT fiber. The CNT returns to its previous position after the nanoprobe retraction, as shown in Movie S1 (Supporting Information).

2.4. Demonstration of 3D Imaging of Overlapped Structures

AFM was initially developed to visualize and study the 2D surface structures of a sample. Technological development further extended the AFM capabilities to provide sample information in three dimensions. To demonstrate that 3D-AFM can simultaneously visualize vertically overlapped 3D nanoscale structures, we fabricated a 3D structure with a suspended CNT fiber and underlying Pt nanodots as displayed in **Figure 4a**. In contrast to the 3D model structure shown in Figure 1, this arrangement features several Pt dots fabricated beneath the CNT to introduce specific target structures. The fabrication process is similar to the steps discussed in Section 2.1. First, a Si substrate with 30 nm gold-coated was used to fabricate two rectangular Pt pillars by EBD technique. Then, Pt dots were fabricated by the same EBD technique and strategically positioned between the two rectangular Pt pillars (the SEM image can be found in Figure S3, Supporting Information). These Pt dots measure less than 100 nm in length and have a diameter of ≈50 nm. It is important to minimize the sample drift as much as possible before the fabrication of Pt dots to precisely position them. Lastly, CNT was picked from the Si cartridge with the W probe and placed carefully on top of the Pt pillars (Figure S3, Supporting Information).

3D-AFM measurement was conducted in dynamic mode within the region highlighted by the yellow box in Figure 4a. The carbon tip used for this measurement is shown in Figure S3 (Supporting Information). The *F-z* curves acquired by the measurement were processed to construct the 3D map of suspended CNT with Pt nanodots. First, decimation was applied to reduce the number of *z* pixels. Then, the unnecessary upper part of the 3D data was cut, and background subtraction was performed with linear fitting. After average filters were applied, the *F-z* curve is shown in Figure 4c, where the strong force peak appeared due to the CNT. At this point, the simple threshold filter is not applicable for extracting the CNT fiber components because there are many cases where the background friction forces exceed the threshold. As a result, we performed differentiation of the force curves and extracted the force gradient distribution (highlighted by blue color in Figure 4d) to visualize the CNT (see Figures S4 and S5, Supporting Information for more details on the data processing and 3D visualization method). The resulting 3D map of the measured volume is presented in Figure 4b, revealing the presence of suspended CNT and Pt nanodots beneath it. The above demonstration provides unambiguous evidence supporting the capability of 3D-AFM to visualize vertically overlapped 3D nanostructures.

3. Conclusion

In this study, we have demonstrated that 3D-AFM can visualize the 3D configuration of vertically overlapped nanoscale structures by imaging a suspended CNT fiber with underlying nanodots and have investigated the mechanism and optimal conditions for such imaging through a combined experimental and computational approach. We have fabricated the 3D model nanostructure featuring suspended CNT on Pt pillars (Figure 1). We designed this model structure large enough to be imaged by SEM while small enough to be observed by 3D-AFM in different operational modes. The 3D-AFM results revealed that the dynamic mode significantly reduces the friction between the AFM nanoprobe, and CNT fiber compared to the static mode (Figure 2). In addition, this friction was further reduced at the second resonance in dynamic mode compared to the first one. This finding will greatly contribute in reducing the disturbance of self-organizing systems while measuring with the 3D-AFM technique.

The Langevin dynamics simulation revealed how the flexible suspended CNT undergoes lateral displacement after repulsive interactions (Figure 3), enhancing our understanding of the imaging mechanism of flexible structures. The simulation further revealed that the continuous vibration of the cantilever in dynamic mode hinders the establishment of stable and robust adhesion between the CNT and nanoprobe. Consequently, this phenomenon results in reduced friction during dynamic mode operations, thereby facilitating the 3D imaging of flexible structures while concurrently minimizing potential damage.

Furthermore, we demonstrated the capability of 3D-AFM to simultaneously observe vertically overlapped nanoscale structures by imaging a suspended CNT fiber with Pt nanodots beneath it (Figure 4). This demonstration not only contributes to a deeper understanding of the mechanism behind the simultaneous imaging of overlapped structures but also instills confidence in the effectiveness of this advanced technique.

Until now, this method has primarily been confined to measuring hydration structures. However, here we have successfully introduced unambiguous evidence to support the feasibility of extending this methodology to the observation of larger-scale flexible 3D structures. In addition, we have provided a detailed comparison between experimental and simulated results, elucidating the theoretical basis for it. As a result, this work would significantly broaden the application scope of 3D-AFM, extending beyond hydration structure measurement to a broad range of 3D self-organizing systems. In particular, since many of the micro/nanostructures in biology are self-organized by individual biomolecules, the advancements made in this study may potentially lead to more detailed and accurate AFM analysis of various 3D biological systems such as cells, organelles, chromosomes, and vesicles.

4. Experimental Section

AFM Nanoprobe Fabrication: The carbon nanoprobes were fabricated on OPUS 240AC cantilever (240 µm length, 3 N m^{-1} spring constant) by the EBD technique in a Helios G4 CX dual beam system (FEI, Thermo Fisher Scientific, USA), as described previously.[25] The carbon gas source was injected from a nearby GIS that used naphthalene ($C_{10}H_8$) as a gas precursor. Then, the deposition was achieved by using an electron beam to dissociate the gas within the area of the scanned beam. The electron beam acceleration voltage was set at 15 kV, the current at 0.17 nA, and the working distance at 4.1 mm. First, the silicon tip of the cantilever was trimmed a bit with FIB to make the fabrication area flat. Then, a few nm thick carbon film was deposited to increase the adhesion of the nanoprobe with the trimmed surface of the tip. Finally, a 2 µm long nanoprobe (120 nm in diameter) was fabricated by depositing carbon for ≈4 min. The cantilever was tilted by 10° for the fabrication to the center axis to compensate for the mounting angle of the AFM cantilever holder.

Sample Preparation: A Si cartridge equipped with CNTs was prepared using the following method by partly referring to previous reports.[31,32] First, Pt was coated on the Si cartridge with a thickness of 30 nm to make it conductive using a dc sputter coater (KST-CSPS-KF1, K's Tech). Next, CNT powder (412988-2G, Sigma–Aldrich) was dissolved in ethanol (14713-95 Nacalai Tesque Inc.) to prepare a CNT suspension. Then, the suspension underwent sonication using an ultrasonic homogenizer (UX-050, MITSUI, equipped with a 3 mm diameter tip and 500 W maximum power capability). After that, 250 µL of the CNT suspension was dropped onto aluminum foil placed on a hot plate. The solution was heated at 400 °C for 30 min to volatilize the ethanol. After 30 min, the Si cartridge was gently traced over the aluminum foil; as a result, CNTs adhered at the edge of the Si cartridge. These are single and multi-walled CNTs with ≈40 nm in diameter and ≈10 µm in length.

The W probe used in the nanomanipulator (EasyLift) was purchased from MicroSupport (102 466), Japan. Before the fabrication of the model CNT structure, the Si substrate was coated with a 30 nm layer of gold by using a dc sputter coater. Then the model CNT structure was fabricated as described in Figure 1. The distance between the structure and the Si substrate's edge was calculated to ensure proper alignment of the tip position during the AFM measurements. The acceleration voltage and working distance in the SEM were kept at 5 kV and 4.1 mm respectively. For the AFM measurements, the CNT structure was put in a 35 mm plastic dish (TPP, Techno Plastic Products AG, Trasadigen, Switzerland) and filled with 2 mL of milli-Q water.

3D-AFM Measurements: The 3D-AFM measurements were performed by JPK Nanowizard 4 BioAFM (Bruker Nano GmbH, Berlin, Germany). The nanoprobe was aligned with the position of the CNT structure and multiple *F-z* curves were measured. The 3D-AFM measurements were

performed in two different manners, the static and dynamic modes. In the static mode, the nanoprobe vertically goes down until it reaches the predefined setpoint. Then, the nanoprobe retracts completely. This mode is also known as QI-mode in JPK system. In the dynamic mode, the nanoprobe vertically goes down while simultaneously oscillating the cantilever at its resonance frequency, with an oscillation amplitude of ≈20 $nm_{p\text{-}p}$. The tip retracts when the cantilever's oscillation amplitude decreases to a certain limit (known as AC-mode force mapping in JPK system). All the measurements were carried out at room temperature (25 °C). Sensitivity and cantilever stiffness were calibrated by the thermal noise method implemented in the JPK system. All AFM data were processed by custom-built LabVIEW (National Instruments, USA) software.

Figure 2e shows the 3D-AFM results obtained in static mode where the force setpoint was 40 nN. Figure 2f presents the 3D-AFM results obtained in the dynamic mode where the cantilever oscillates at its first resonance frequency with an oscillation amplitude of 20 $nm_{p\text{-}p}$. The excitation frequency was 27.48 kHz, and the amplitude set point was 56%. Figure 2g presents the 3D-AFM results obtained in the dynamic mode where the cantilever oscillates at its second resonance frequency with the same oscillation amplitude. The excitation frequency was 163.41 kHz, and the amplitude setpoint was 75%. The measured volume in Figure 2e–g were 0.5 × 0.5 × 3 μm^3 with 32 × 32 × 3000 pixels. The vertical approaching and retracting speed of the nanoprobe was 30 μm s^{-1}. All the measurements in Figure 2e–g were done exactly in the same area of the CNT.

The 3D-AFM map displayed in Figure 4 was acquired in the first resonance dynamic mode where the free oscillation amplitude was 20 $nm_{p\text{-}p}$. The excitation frequency was 28.34 kHz and the amplitude setpoint was 47%. The measured volume was 0.5 × 0.5 × 3 μm^3 with 64 × 64 × 3905 pixels. The vertical approaching and retracting speeds of the nanoprobe were 30 and 50 μm s^{-1} respectively. Voxler 3 (Golden Software) was used for the 3D visualization of the CNT with underlying Pt nanodots shown in Figure 4b.

Computational Details to Simulate 3D-AFM Images of a CNT Fiber: The system was composed of a single CNT fiber and an AFM probe. A bead-spring CNT model[33] was employed for the CNT fiber; that is, the total energy representing the CNT fiber is the sum of bond energy, bending energy, and the Lennard-Jones potential. The following parameters were modified from the double wall CNT parameters in reference[33] to mimic the thick CNT of 30 nm diameter in water. The equilibrium distance between beads (r_0 in reference[33]) was changed to 30 nm. The spring constant of the bending energy (k_B in reference[33]) was increased by a factor of ten (900,000 kcal mol^{-1} rad^{-2}) to account for thickness. Since ε_{LJ} of the Lennard-Jones potential is considered to be decreased because of the screening of water, three smaller values (10, 20, and 36 kT, where k and T are the Boltzmann constant and the temperature, respectively) than the original value in reference[33] (72 kT) were tested to find an appropriate one (Figure S6, Supporting Information). The experimental results were best reproduced when ε_{LJ} = 10 kT (20 kT may be a possible choice). The number of beads in the CNT model was 50, and they were placed at y = 30 to 1,500 nm at each 30 nm. The particles at both ends of CNT were harmonically fixed at the initial positions with a spring constant of 10^{-23} kcal mol^{-1} nm^{-2} to mimic the experimental setup.

A taper shape probe model was developed with a smooth to rough surface. The cone angle of the model was 10 degrees: the radius of the probe at the tip end was 15 nm at z = 0 nm and linearly increased up to 60 nm at z = 514.35 nm. This shape is almost the same as that used in the experiments. The smoothness (or roughness) was mimicked by the spacing between beads in the probe: the surface is rough when the spacing is large (see Figure S7, Supporting Information). Four spacing values of 6, 12, 18, and 30 nm were examined to find an appropriate one to mimic the surface roughness of the probe (Figure S7, Supporting Information). The spacing of 12 nm was found to best reproduce the experimental results (6 nm may be a possible choice). As an interaction between the CNT fiber and probe, the shifted Lennard-Jones potential[34] (V_{shift}) was employed:

$$V_{shift}(r) = 4\varepsilon_{LJ}\left\{\left(\frac{\sigma_{LJ}}{r - r_{shift}}\right)^{12} - \left(\frac{\sigma_{LJ}}{r - r_{shift}}\right)^{6}\right\} \quad (1)$$

where r_{shift} is to describe the excluded volume of the probe while keeping the attraction small between CNT and probe represented by σ_{LJ} (2 nm, which is slightly larger than the original parameter in reference[33] (1.97 nm)). Since $r_{shift} + \sigma_{LJ}$ is the sum of the CNT fiber and probe radii, r_{shift} was set to 73 nm.

The Langevin equation of motion was solved to evolve the time.[35] The temperature was set to 300 K. The effective mass of beads (m) should include the hydrodynamic viscosity of CNT fiber in water, but this value is currently unknown. As such, m of 0.2, 2, 20, 200 ng were examined and found that m of 20 ng best reproduces experimental results. All the parameters that best reproduce the experiments were tabled (Table S1, Supporting Information) and were used to simulate all the figures in the main text. The time step was 10 ns for m = 0.2 and 2 ng and 100 ns for m = 20 and 200 ng.

The mechanism to move the probe was described in the previous paper[35]: the probe was moved by the following equation,

$$z_{tip} = z_0 - \nu_{scan}t + A/2 \sin \omega t \quad (2)$$

where z_{tip}, z_0, ν_{scan}, t, A, and ω are the z-coordinate of the tip, the initial height of the tip, the vertical scanning velocity, time, the peak-to-peak amplitude of the oscillation, and the frequency of the oscillation, respectively. ν_{scan}, A, and ω were set to 30 μm s^{-1}, 20 nm, and 25 kHz, respectively, which were the same as those in the experiments. The geometry of the beads in the probe was fixed in the simulation since the AFM probe with a diameter of 120 nm was assumed to be much more rigid than CNT with a 30 nm diameter.

When simulating a force-distance curve, the probe was initially located above the center of the CNT fiber (x = 0). When simulating a sliced 3D-AFM image at the center of CNT, the initial x position of the probe was changed from −250 to 250 nm by 5 nm to calculate 101 curves. To simulate the force versus distance curves, the previously developed method where the Jarzynski equality was solved was used.[36] All the codes to simulate force versus distance curves were developed. All snapshots and movies were produced using the Visual Molecular Dynamics package.[37]

Supporting Information

Supporting Information is available from the Wiley Online Library or from the author.

Acknowledgements

This work was supported by the World Premier International Research Center Initiative, Ministry of Education, Culture, Sports, Science and Technology, Japan; KAKENHI No. 21H05251 and 20H00345, Japan Society for the Promotion of Science and Precursory Research for Embryonic Science and Technology JPMJPR20K6, Japan Science and Technology Agency. The simulations were carried out on the supercomputers at the Research Center for Computational Science in Okazaki, Japan (Project: 23-IMS-C101).

Conflict of Interest

The authors declare no conflict of interest.

Data Availability Statement

The data that support the findings of this study are available from the corresponding author upon reasonable request.

Keywords

3D atomic force microscopy, carbon nanotube, flexible structure, hydration structure

Received: February 27, 2024
Revised: June 6, 2024
Published online:

[1] S. Su, J. Zhao, T. H. Ly, *Small Methods* **2024**, 202400211.
[2] C. Chitty, K. Kuliga, W. F. Xue, *Biochem. Soci. Trans.* **2024**, *52*, 761.
[3] T. Fukuma, Y. Ueda, S. Yoshioka, H. Asakawa, *Phys. Rev. Lett.* **2010**, *104*, 016101.
[4] T. Fukuma, R. Garcia, *ACS Nano* **2018**, *12*, 11785.
[5] K. Kobayashi, N. Oyabu, K. Kimura, S. Ido, K. Suzuki, T. Imai, K. Tagami, M. Tsukada, H. Yamada, *J. of Chem. Phys.* **2013**, *138*, 184704.
[6] K. Umeda, L. Zivanovic, K. Kobayashi, J. Ritala, H. Kominami, P. Spijker, A. S. Foster, H. Yamada, *Nat. Commun.* **2017**, *8*, 2111.
[7] D. Martin-Jimenez, E. Chacon, P. Tarazona, R. Garcia, *Nat. Commun.* **2016**, *7I*, 12164.
[8] K. Miyazawa, N. Kobayashi, M. Watkins, A. L. Shluger, K. I. Amano, T. Fukuma, *Nanoscale* **2016**, *8*, 7334.
[9] H. Söngen, C. Marutschke, P. Spijker, E. Holmgren, I. Hermes, R. Bechstein, S. Klassen, J. Tracey, A. S. Foster, A. Kühnle, *Langmuir* **2017**, *33*, 125.
[10] S. Benaglia, M. R. Uhlig, J. Hernández-Muñoz, E. Chacón, P. Tarazona, R. Garcia, *Phys. Rev. Lett.* **2021**, *127*, 196101.
[11] P. J. Molino, D. Yang, M. Penna, K. Miyazawa, B. R. Knowles, S. MacLaughlin, T. Fukuma, I. Yarovsky, M. J. Higgins, *ACS Nano* **2018**, *12*, 11610.
[12] A. Yurtsever, P. X. Wang, F. Priante, Y. M. Jaques, K. Miyata, M. J. MacLachlan, A. S. Foster, T. Fukuma, *Small Methods* **2022**, *6*, 2200320.
[13] H. Asakawa, S. Yoshioka, K. I. Nishimura, T. Fukuma, *ACS Nano.* **2012**, *6*, 9013.
[14] E. T. Herruzo, H. Asakawa, T. Fukuma, R. Garcia, *Nanoscale* **2013**, *5*, 2678.
[15] K. Umeda, K. Kobayashi, N. Oyabu, K. Matsushige, H. Yamada, *Nanotechnology* **2015**, *26*, 285103.
[16] K. Kuchuk, U. Sivan, *Nano Lett.* **2018**, *18*, 2733.
[17] M. Tsukada, N. Watanabe, M. Harada, K. Tagami, *J. Vac. Sci. Tech. B.* **2010**, *28*, C4C1.
[18] M. Watkins, M. L. Berkowitz, A. L. Shluger, *Phys. Chem. Chem. Phys.* **2011**, *13*, 12584.
[19] B. Reischl, M. Watkins, A. S. Foster, *J. Chem. Theo. Comput.* **2013**, *9*, 600.
[20] M. Watkins, B. Reischl, *J. Chem. Phys.* **2013**, *138*, 154703.
[21] K. I. Amano, K. Suzuki, T. Fukuma, O. Takahashi, H. Onishi, *J. Chem. Phys.* **2013**, *139*, 224710.
[22] T. Fukuma, B. Reischl, N. Kobayashi, P. Spijker, F. F. Canova, K. Miyazawa, A. S. Foster, *Phys. Rev. B.* **2015**, *92*, 155412.
[23] K. Miyazawa, J. Tracey, B. Reischl, P. Spijker, A. S. Foster, A. L. Rohl, T. Fukuma, *Nanoscale* **2020**, *12*, 12856.
[24] K. Suzuki, K. Kobayashi, N. Oyabu, K. Matsushige, H. Yamada, *J. Chem. Phys.* **2014**, *140*, 054704.
[25] M. Penedo, K. Miyazawa, N. Okano, H. Furusho, T. Ichikawa, M. S. Alam, K. Miyata, C. Nakamura, T. Fukuma, *Sci. Adv.* **2021**, *7*, eabj4990.
[26] T. Ikarashi, T. Yoshino, N. Nakajima, K. Miyata, K. Miyazawa, Y. Morais Jaques, A. S. Foster, M. Uno, C. Takatoh, T. Fukuma, *ACS Appl. Nano Mater* **2021**, *4*, 71.
[27] T. Ikarashi, K. Nakayama, N. Nakajima, K. Miyata, K. Miyazawa, T. Fukuma, *ACS Appl. Mater. Interfaces* **2022**, *14*, 44947.
[28] K. Umeda, K. Kobayashi, H. Yamada, *Nanoscale* **2022**, *14*, 4626.
[29] T. Sumikama, *Biophys. Rev.* **2023**, *15*, 2059.
[30] R. Garcia, R. Perez, *Surf. Sci. Rep.* **2002**, *47*, 197.
[31] Y. Nakayama, S. Akita, *New J. of Phys.* **2003**, *5*, 128.
[32] H. Maruyama, T. Ishibashi, K. Hirahara, Y. Nakayama, *Appl. Phys. Express* **2010**, *3*, 025101.
[33] S. Cranford, H. Yao, C. Ortiz, M. J. Buehler, *J. Mech. Phys. Solids* **2010**, *58*, 409.
[34] P. A. Tillman, D. R. Rottach, J. D. McCoy, S. J. Plimpton, J. G. Curro, *J. Chem. Phys.* **1997**, *107*, 4024.
[35] T. Sumikama, A. S. Foster, T. Fukuma, *J. Phys. Chem. C* **2020**, *124*, 2213.
[36] T. Sumikama, T. Fukuma, F. F. Canova, D. Z. Gao, M. Penedo, K. Miyazawa, A. S. Foster, *J. of Phys. Chem. Lett.* **2022**, *13*, 5365.
[37] W. Humphrey, A. Dalke, K. Schulten, *VMD: Vis. Mol. Dyna.* **1996**, *14*, 33.

